Direct observation of the energy gain underpinning ferromagnetic superexchange in the electronic structure of CrGeTe₃

Matthew D. Watson [1,*], Igor Marković [1,2], Federico Mazzola,[1] Akhil Rajan [1], Edgar A. Morales,[1,2] David M. Burn [3],
Thorsten Hesjedal [4], Gerrit van der Laan [3], Saumya Mukherjee [5], Timur K. Kim,[5] Chiara Bigi [6,7], Ivana Vobornik,[6]
Monica Ciomaga Hatnean [8], Geetha Balakrishnan [8], and Philip D. C. King [1,†]

[1]*SUPA, School of Physics and Astronomy, University of St Andrews, St Andrews KY16 9SS, United Kingdom*
[2]*Max Planck Institute for Chemical Physics of Solids, Nöthnitzer Strasse 40, 01187 Dresden, Germany*
[3]*Magnetic Spectroscopy Group, Diamond Light Source, Didcot OX11 0DE, United Kingdom*
[4]*Department of Physics, Clarendon Laboratory, University of Oxford, Oxford OX1 3PU, United Kingdom*
[5]*Diamond Light Source, Harwell Campus, Didcot OX11 0DE, United Kingdom*
[6]*Istituto Officina dei Materiali (IOM)-CNR, Laboratorio TASC, Area Science Park, S.S.14, Km 163.5, 34149 Trieste, Italy*
[7]*Department of Physics, University of Milano, 20133 Milano, Italy*
[8]*Department of Physics, University of Warwick, Coventry CV4 7AL, United Kingdom*

We investigate the temperature-dependent electronic structure of the van der Waals ferromagnet, CrGeTe₃. Using angle-resolved photoemission spectroscopy, we identify atomic- and orbital-specific band shifts upon cooling through T_C. From these, together with x-ray absorption spectroscopy and x-ray magnetic circular dichroism measurements, we identify the states created by a covalent bond between the Te $5p$ and the Cr e_g orbitals as the primary driver of the ferromagnetic ordering in this system, while it is the Cr t_{2g} states that carry the majority of the spin moment. The t_{2g} states furthermore exhibit a marked bandwidth increase and a remarkable lifetime enhancement upon entering the ordered phase, pointing to a delicate interplay between localized and itinerant states in this family of layered ferromagnets.

I. INTRODUCTION

The recent discovery of long-range ferromagnetic order in single/bilayer transition metal chalcogenides and halides [1,2] has opened new opportunities for studying fundamental questions in magnetism [3], and has provided a powerful and highly tunable platform for the engineering of magnetic interactions [3,4] and for the creation of novel device structures [5–7]. Typically, such two-dimensional magnets are realized by isolating individual layers of magnetic van der Waals materials systems. Even in the parent bulk compounds, however, the microscopic origins and nature of their magnetic ordering has proved controversial, and key quantities such as how the underlying electronic structure evolves into the magnetic state remains completely unexplored to date. In this work, we show how such electronic structure information, extracted from temperature-dependent angle-resolved photoemission spectroscopy (ARPES), can be used to provide a direct probe of atomic- and orbital-specific energy gains underpinning the magnetic ordering.

We focus here on CrGeTe₃, a ferromagnetic semiconductor with a T_C of ≈ 63 K in its bulk form [8–10]. The transition temperature decreases with reducing thickness, but long-range ferromagnetic order persists down to the bilayer (i.e., when the

material is thinned such that it hosts only two Cr-containing layers stacked along the out-of-plane direction) [2]. Its crystal structure [Fig. 1(a)] can be considered as a variation on the CdI₂-type layered *1T* transition metal dichalcogenides [11]. Compared to metastable *1T*-CrTe₂ [12], however, one-third of the Cr sites are replaced by Ge dimers. Within a simple ionic picture, the remaining Cr ions are thus in a more stable 3+ nominal charge state, and are arranged in a honeycomb lattice, similar to the CrX₃ trihalide family [13].

II. METHODS

Single crystals of CrGeTe₃ were grown using Te as a flux following previously reported procedures [9]. The crystals were separated from the flux by centrifuging at 500 °C and the resulting crystal platelets were cleaned free of any excess Te. The crystals were found to exhibit a sharp magnetic transition at ∼65 K [see Fig. SM1 in the Supplemental Material (SM) [14]] in good agreement with previous literature reports [10]. ARPES measurements were performed at beamlines APE-LE at Elletra, Italy and I05 at Diamond Light Source, UK. Single crystal samples were cleaved *in situ*, and ARPES measurements were performed using *p*-polarized photons (photon energies specified in the figure captions) at sample temperatures between 25 and 150 K.

Since CrGeTe₃ is a semiconductor with a resistivity that becomes large at low temperatures [9], charging of the sample due to the emission of photoelectrons can becomes a

---

*matthew.watson@diamond.ac.uk
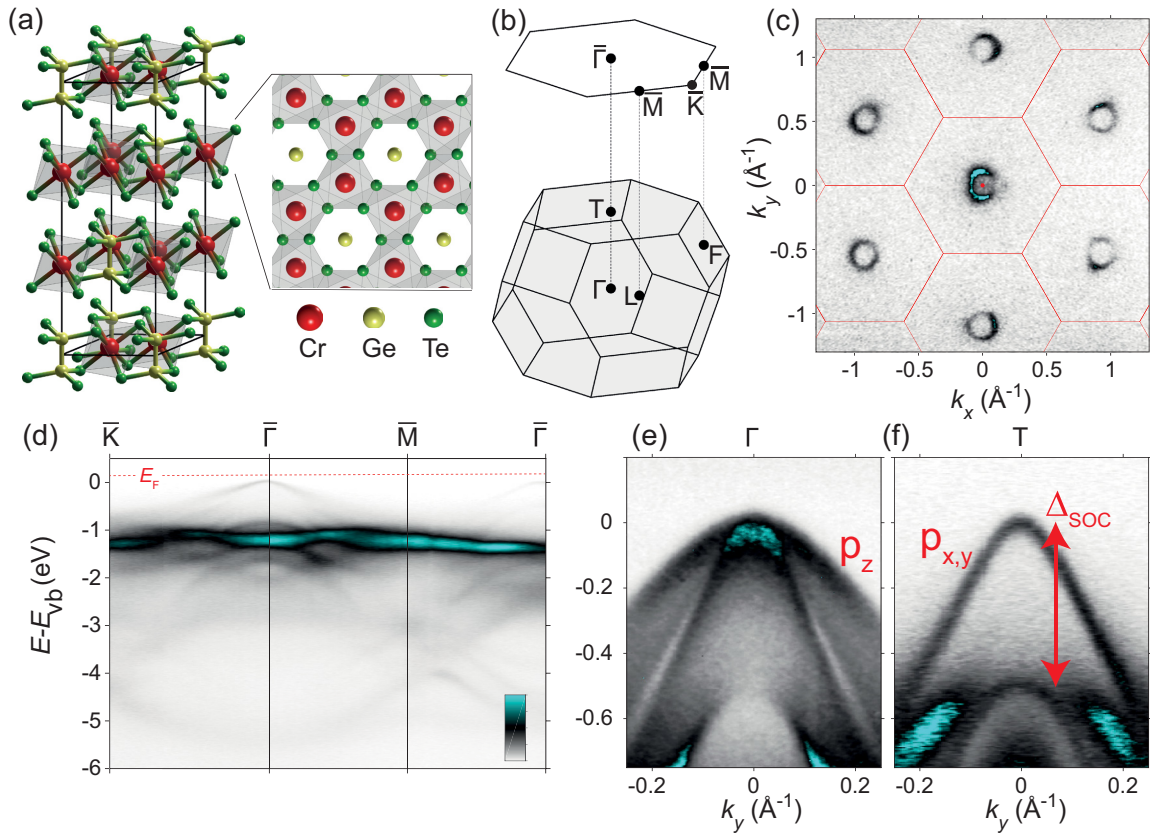†philip.king@st-andrews.ac.uk

FIG. 1. Paramagnetic electronic structure of CrGeTe$_3$. (a) Crystal structure of CrGeTe$_3$, with trilayer stacking in the unit cell, and (b) corresponding 3D Brillouin zone. High-symmetry points are shown, as well as their projection into the hexagonal surface Brillouin zone (barred notation). (c) ARPES intensity map ($h\nu = 80$ eV) at an energy 0.1 eV below the top of the valence band, showing slightly trigonally warped contours derived from $p_{x/y}$ states located at each $\bar{\Gamma}$ point. (d) ARPES dispersion measured ($h\nu = 80$ eV) along high-symmetry directions of the surface Brillouin zone, over an extended binding energy range. A pronounced state with only weak dispersion is evident in addition to the strongly dispersive states. The energy scale is referenced to the valence band maximum, E_{vb}; the chemical potential lies within the band gap, and for the sample shown here is located 0.165 eV above the valence band top (dashed red line). (e),(f) Detailed valence band dispersions at high-symmetry points of the 3D Brillouin zone [(e) Γ, $h\nu = 22$ eV; (f) T, $h\nu = 61$ eV]. The p_z band disperses significantly along k_z such that it is at higher binding energies than the range shown in (f) for the T point. All data are measured in the paramagnetic phase at $T = 100$ K.

restrictive issue. In practice, we found that certain regions of the sample suffered less from charging than others, despite having the same band features at higher temperature. This is presumably due to local variations in the residual conductivity, and thus ease of replenishing the photocurrent. We further reduced the beamline flux to a very low value. In this way, we were able to measure the temperature-dependent electronic structure down to $T \approx 40$ K with negligible shifting of the bands when doubling the photon flux (indicating an absence of charging). Below 40 K we were not able to fully avoid sample charging effects, but in the worst case, in our data taken at $T = 25$ K and $h\nu = 61$ eV, only a moderate rigid shift of the bands (≈ 55 meV) was observed when doubling the flux, without significant broadening of the features of interest. By analyzing only the lowest-flux data and also consistently referencing the energy scale to the valence band maximum, the sample charging effects are mitigated in the data presented here.

X-ray absorption spectroscopy (XAS) and x-ray magnetic circular dichroism (XMCD) measurements were performed in the high-field magnet end-station on beamline I10 at Di-

amond Light Source. The sample was cleaved *in situ* in the preparation chamber and transferred under ultrahigh vacuum to the high-field magnet chamber. Spectra were measured with 100% left- and right-circularly polarized light in total-electron yield detection, which probes the top 3–5 nm of the sample [15]. The XMCD measured as a function of field showed that at 20 K the sample magnetization saturates at ∼0.5 T. A field of 2 T was used for the measurements shown here. A reference sample of Cr$_2$O$_3$ was measured to provide an energy calibration, as well as to confirm that the measured CrGeTe$_3$ is free from surface oxidation.

Atomic multiplet theory calculations were employed to calculate the Cr $L_{2,3}$ XAS and XMCD spectra using the electric-dipole transitions $3d^n \rightarrow 2p^5 3d^{n+1}$, where the spin-orbit and electrostatic interactions are treated on an equal footing [16,17]. The wave functions of the initial- and final-state configurations are calculated in intermediate coupling using Cowan's atomic Hartree-Fock (HF) code with relativistic corrections [18,19]. The atomic electrostatic interactions include the $3d$-$3d$ and $2p$-$3d$ Coulomb and exchange interactions, which are reduced to 80% and 75%,

respectively, of their atomic HF value to account for the intra-atomic screening [16]. Hybridization effects are included by mixing the Cr $3d^3$ and $3d^4\underline{L}$ wave functions, where $\underline{L}$ represents a hole on the neighboring atoms in states of appropriate symmetry. The charge-transfer energies in the initial and final state are $E(3d^4\underline{L}) - E(3d^3) = -1$ eV and $E(2p^53d^5\underline{L}) - E(2p^53d^4) = -3$ eV, respectively. Note that a negative "charge transfer energy" here in the initial state implies that the average energy of the $E(3d^4\underline{L})$ configuration is lower; similarly negative values were used for $Cr_{1-\delta}Te$ [20]. An octahedral crystal field of $10Dq = 1.8$ eV was included. The hybridization parameter $T = \langle \psi(d^3)|H|\psi(d^4\underline{L}) \rangle$ was 1.7 eV. The calculated Cr L_3 (L_2) line spectra are convoluted by a Lorentzian with a half width of $\Gamma = 0.2$ eV (0.4 eV) for the intrinsic lifetime broadening and a Gaussian with a standard deviation of $\sigma = 0.15$ eV for the instrumental broadening.

III. RESULTS

Our ARPES measurements within the paramagnetic state above T_C are shown in Fig. 1. Consistent with previous studies [21–24], these indicate that the uppermost valence bands are comprised of a set of highly dispersive states, derived from the Te $5p$ orbitals [Figs. 1(c)–1(f)]. Very similar to the $1T$ transition metal dichalcogenides [25], the $5p_{x,y}$ orbitals form a pair of quasi-2D states at the valence band top, which are separated by a strong spin-orbit splitting of $\approx$500 meV [Fig. 1(f)]. Additionally, there is a $5p_z$-derived state which has a strong out-of-plane dispersion, reaching a maximum at the bulk Γ point [Fig. 1(e)].

Here, we focus on the deeper-lying states. Around 0.8–1.5 eV below the top of the valence bands we observe a set of flat bands [Fig. 1(d)]. Their spectral weight is particularly pronounced when measured using photon energies which are tuned into resonance with the core Cr $3p$ to $3d$ transition: they are barely visible when measured using off-resonant photon energies just below this M-edge transition in Fig. 2(a), but dominate the spectrum on resonance [Fig. 2(b)], before returning to a lower intensity for photon energies above the transition [2(c)]. This reflects a resonant enhancement of photoemission intensity from states with Cr d-orbital character [26]. Quantitative analysis of the spectral weight associated with these states [Fig. 2(d), red points] allows us to identify the flat bands as having almost entirely Cr $3d$ character.

In the simplest picture for Cr^{3+} with a $3d^3$ configuration, and thus a half-filled t_{2g} shell [Fig. 3(f)], metallic Cr-derived states would be expected at the Fermi level. From our resonant-ARPES measurements, it is clear that the uppermost Cr-derived states, which we thus assign as t_{2g} states [27], are located around 1 eV below the valence band maximum, E_{vb}. This reflects how on-site Coulomb repulsion terms ensure the t_{2g} shell remains locally spin polarized even in the paramagnetic phase, although without long-range order of the spin orientation. Nonetheless, the relatively small binding energy of these states, their small but finite dispersion, and the fact that they remain rather sharp and not completely incoherent in our measurements [Fig. 1(d)] indicates that the effective on-site Coulomb term is somewhat modest in this system. The overall appearance of this t_{2g} manifold is in strong contrast
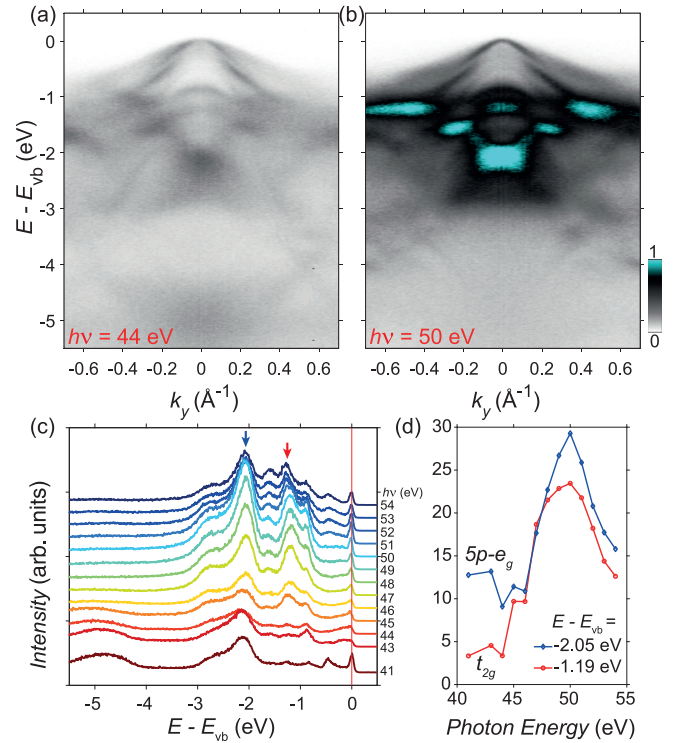

FIG. 2. Resonant ARPES measurements. (a),(b) ARPES measurements in the paramagnetic state ($T = 80$ K) (a) off ($h\nu = 44$ eV) and (b) on ($h\nu = 50$ eV) resonance with the Cr $3p$ to $3d$ transition. The color map is fixed to the same intensity range in both plots, highlighting the extra intensity from the Cr $3d$ weight on resonance. (c) Photon energy-dependent energy distribution curves (EDCs) measured at $\overline{\Gamma}$ as a function of photon energy across the resonance. (d) The photon energy-dependent spectral weight of peaks located 1.19 eV and 2.05 eV below the valence band top [arrows in (c)], identify the near pure Cr (t_{2g}) and partial Cr (e_g) character of the corresponding states, indicating that the latter are hybridized with Te $5p$ states.

with that observed in, e.g., $PdCrO_2$, where t_{2g} states of Cr^{3+} form a Mott-insulating subsystem and give rise to a very broad band of incoherent excitations at a higher binding energy of 2 eV [28]. Thus, although the local Coulomb repulsion terms are relevant for understanding the physics of $CrGeTe_3$, the material does not reach the limit of fully localized and totally incoherent excitations as suggested by recent dynamical mean field theory calculations [21]. Instead, we suggest that the "local band theory" [29] or the "disordered local moment" technique [30] could be more appropriate theoretical approaches to describing the paramagnetic phase of $CrGeTe_3$.

Our resonant-ARPES measurements also reveal an additional state located at $\approx$2 eV below the valence band maximum which exhibits a roughly twofold spectral weight enhancement at the Cr M-edge resonance [blue points in Fig. 2(d)]. While less pronounced than for the resonant enhancement of the t_{2g} states, our measurements still point to a partial Cr-derived character of this higher binding-energy state. We attribute this to the breakdown of an ionic picture for $CrGeTe_3$. The extensive $5p$ orbitals of Te significantly overlap with the Cr e_g orbitals [Fig. 3(e)], and can be expected to form strongly covalent bonding and antibonding states [31,32]. The
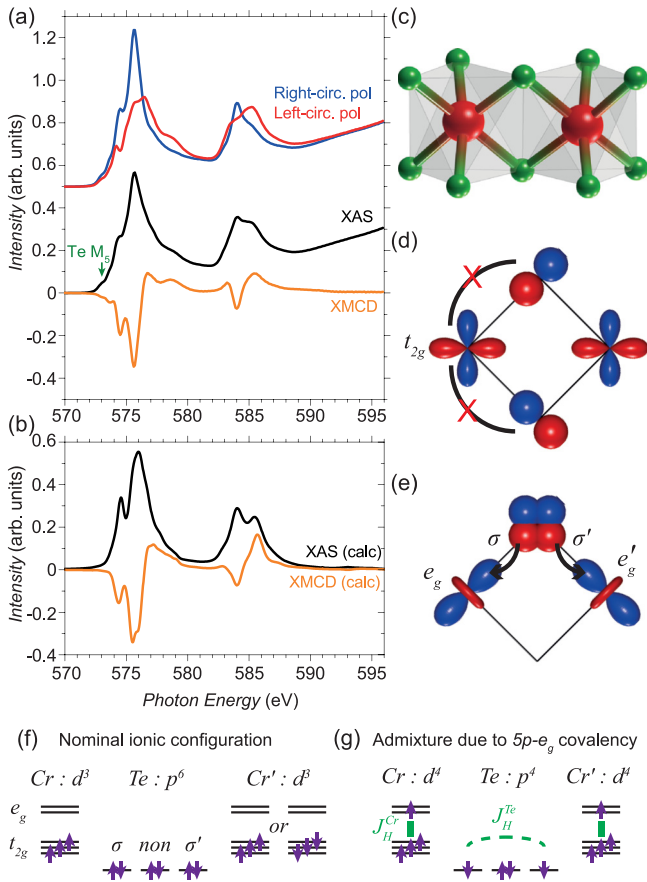
FIG. 3. Evidence for partial occupation of the e_g orbitals from XAS and XMCD. (a) Dichroic absorption spectra for the Cr $L_{2,3}$ edges measured in an applied field of 2 T, which saturates the magnetization (see methods). (b) Simulation of XAS and XMCD from multiplet calculations, reproducing the essential features of the experimental spectra. (c) Edge-sharing CrTe$_6$ octahedra. (d) For perfect octahedra and exact bond angles, σ hopping is forbidden from the $5p$ to the t_{2g} states by symmetry. (e) In contrast, at least one of the e_g orbitals is available for σ hopping. (f) Schematic representation of the nominal ionic configuration of two adjacent Cr atoms and one of the two intermediary Te atoms. The orbitals are defined as in (d),(e) with *non* representing an additional nonbonding $5p$ state. (g) Corresponding orbital configuration for a state that additionally hosts a significant $5p\sigma - e_g$ covalent bonding. The unpaired spins on the Te site interact according to J_H^{Te}, which gives an energy gain for on-site alignment of spins; this process thus mediates a net ferromagnetic superexchange between the Cr sites.

bonding states will be fully occupied, while the antibonding states will form the unoccupied conduction band.

To confirm this, in Fig. 3(a) we show x-ray absorption spectroscopy (XAS) and x-ray magnetic circular dichroism (XMCD) measurements at the Cr $L_{2,3}$ edge (see methods). Compared to a reference sample of Cr$_2$O$_3$ (Cr^{3+}, d^3), we find that the Cr $L_{2,3}$ edge of CrGeTe$_3$ is shifted to lower photon energies (Fig. SM2 in SM [14]). Qualitatively, this indicates a higher d-electron count in CrGeTe$_3$ as compared to Cr$_2$O$_3$. Additional insight can be gained by comparison with atomic multiplet calculations (see Methods). To obtain the good agreement between the measured and calculated XAS shown

in Fig. 3(b) necessitated treating the ground state of Cr as a hybridized state with approximately 50% d^3 and 50% d^4 character, corresponding to a d-electron count of $n_d \approx 3.5$. This simultaneously reproduces the measured XMCD spectrum, for which we observe a very strong dichroism [Fig. 3(a)], and for which our calculations yield physically reasonable values for the Cr ground state orbital moment of $m_L = -0.022\mu_B/$Cr and effective spin moment $m_S = 2.81\mu_B/$Cr (i.e., 0.80 μ_B per $3d$ electron).

Further evidence for the hybridization of Cr d states with Te $5p$ states comes from the observation of an additional peak in the XAS which we attribute to the Te M_5 edge. This is challenging to observe in Cr-based materials as the Te M_5 edge lies close in energy to the Cr L_3 edge, which will have a significantly larger intensity [33]. Nonetheless, in both the XAS and XMCD spectra, we find a small peak at 573 eV, which agrees well with the energy at which the Te M_5 edge is expected [green arrow in Fig. 3(a)]. The absence of such a feature in XAS measurements of CrI$_3$ [34,35] support that the peak observed at 573 eV here is indeed from the Te M_5 edge. This directly indicates the presence of empty Te $5p$ states above the Fermi level, since the electric-dipole transitions from $3d$ initial states are only allowed to p and f final states.

On the basis of the XAS, XMCD, and resonant ARPES measurements, we thus attribute the state evident in our ARPES measurements at ≈ 2 eV below the valence band top as a bonding $5p - e_g$ hybridized state. As shown in Figs. 4(a)–4(d), these $5p - e_g$ states at Γ shift to lower energy below T_C. The large magnitude of the shift ($\sim$130 meV), and its sharp onset at T_C, are indicators that this state is the leading candidate for driving the ferromagnetic ordering in this system. In contrast, the Cr t_{2g} states exhibit more gradual shifts. These begin at temperatures above T_C, and [from examining the overall spectra, and from analysis of EDCs at momenta away from the high-symmetry point, e.g., Figs. 4(e) and 4(f)] mostly reflect an increase in bandwidth of the t_{2g} states with decreasing temperature, rather than a rigid band shift.

The dichotomy in the temperature-dependent evolution of the $5p - e_g$ and t_{2g} states through T_C provides important insights into the exchange mechanism underpinning ferromagnetism in CrGeTe$_3$. The long Cr-Cr bond length (3.944 Å) means that direct exchange will be minimal. Moreover, for the edge-sharing octahedral geometry here [Fig. 3(c)], with the Cr-Te-Cr bond angle being very close to 90° [8,9], the formation of σ bonds between the t_{2g} orbitals and the anions is strongly suppressed [Fig. 3(d)] [36]. Given this, for the nominal ionic configuration represented in Fig. 3(f), there would be no mechanism to link the spin directions of the t_{2g} shells of neighboring Cr sites. However, the $5p - e_g$ hybridization identified above is fully symmetry allowed [Fig. 3(e)]. The observation of the corresponding hybridized state in both our ARPES and XAS/XMCD measurements indicates how, beyond the nominal ionic configuration, there is also a significant occupation of orbital configurations with an electron in the e_g shell and a hole in the corresponding σ Te orbital [3(g)].

This provides a natural route to mediate the magnetic interactions via a superexchange mechanism involving the Te atoms. Due to the strong Hund's rule coupling on the Cr sites, the e_g state must be occupied parallel to the local
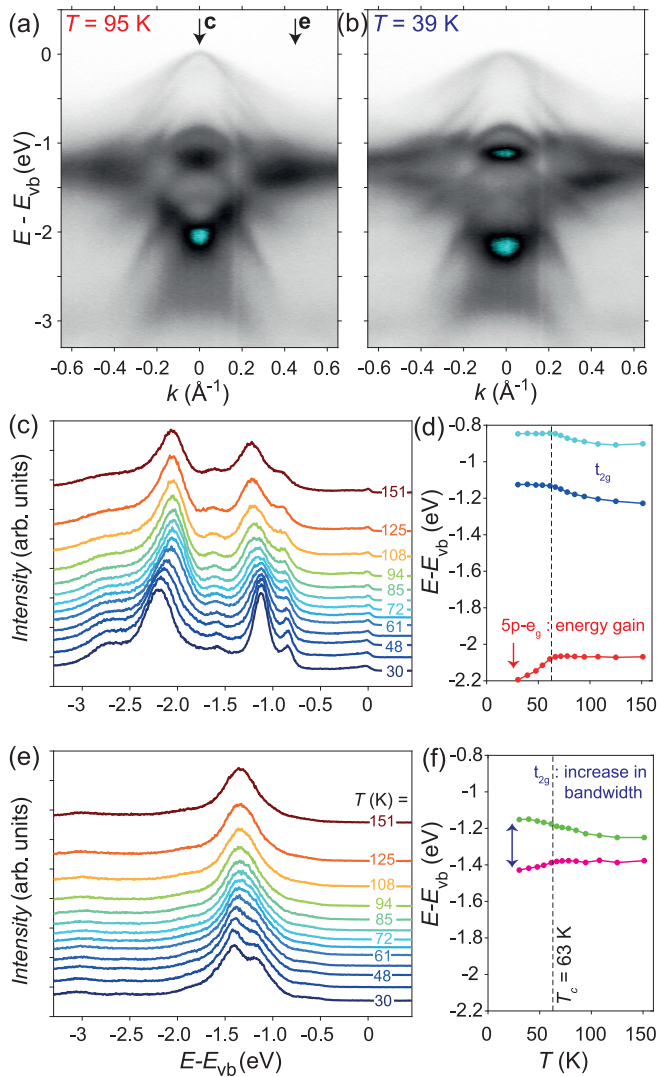
FIG. 4. Temperature-dependent band shifts. (a),(b) ARPES measurements through the Γ point ($h\nu = 48$ eV, also on resonance) (a) above and (b) below T_C. (c) Temperature-dependent EDCs at Γ and (d) corresponding band positions extracted from fitting these EDCs. (e),(f) Equivalent (e) EDCs and (f) band positions at $k = 0.4$ Å^{-1} [see arrow in (a)].

spin orientation of the t_{2g}. When two such bonds are formed simultaneously towards the two neighboring Cr atoms, as shown in Figs. 3(e) and 3(g), the unpaired electrons in orthogonal σ and σ' orbitals also interact on the Te site, according to the Hund's rule J_H^{Te}. This therefore gives an energetic incentive for the development of a net spin moment on the Te sites, antiparallel to the neighboring Cr sites, and overall mediating a ferromagnetic alignment of spins between the Cr sites. Such an antiparallel spin moment on the Te sites is consistently found in DFT calculations of the magnetic ground state [31,32]. Consistent with this, we note that the Te M_5 x-ray absorption edge discussed above [Fig. 3(a)] exhibits a negative XMCD signal, with the same sign as the Cr L_3 edge. Since the azimuthal quantum numbers for the orbitals in these two electric-dipole transitions are opposite (Te $3d \rightarrow 5p$ and Cr $2p \rightarrow 3d$, respectively), this means that the Te and Cr moments are aligned antiparallel.

The above discussions advance a description of the magnetic ordering in CrGeTe$_3$ via a double exchange mechanism, since both kinetic (delocalization of $5p$ orbitals) and potential (Hund's coupling on both sites) terms are involved. Indeed, it can be considered as a classic example of how superexchange generally favors ferromagnetism when the relevant bond angles are nearly $90°$ [37]. As it necessarily involves two separate anion orbitals, it is a weaker interaction than the standard $180°$ superexchange mechanism involving only one anion orbital, consistent with the much lower transition temperature in CrGeTe$_3$ than, e.g., antiferromagnetic LaCrO$_3$ ($T_N = 295$ K). The important role of ligand orbitals in understanding the ferromagnetic superexchange was also recently highlighted in Refs. [31,35,38,39], but here we are able to verify the dominance of the Te $5p$-mediated exchange mechanism by identifying a key experimental signature, i.e., the energy lowering of the bonding $5p - e_g$ state below T_C [Fig. 4(d)]. This is a signature of the Hund's energy gain on the Te site between pairs of these bonding states, and in fact our measurements here can be taken as one of the most direct confirmations to date of the validity of Kanamori's elegant reasoning regarding $90°$ superexchange [37].

The resulting emergence of long-range magnetic order below T_C leaves several other intriguing fingerprints in the spectral function. The first is the increase in bandwidth of the t_{2g} states below T_C [Fig. 4(f)]. Although $pd\sigma$ hoppings are geometrically suppressed for the t_{2g} states (forbidden in the case of perfect octahedra), direct dd (and some $pd\pi$) hopping processes are still allowed. Thus, in the ferromagnetic ground state, the t_{2g} states hybridize to a limited degree, developing a finite dispersion [Fig. 4(b)]. As discussed above, in the paramagnetic state above T_C, the local $S \approx 3/2$ moment is still formed but fluctuations destroy long-range order. A large energy penalty is thus incurred due to the Hund's interaction if an electron hops onto a neighboring site with a different spin orientation. The effective dd hopping processes will therefore be suppressed, consequently narrowing the t_{2g} bandwidth. Experimentally, we find that the bandwidth evolves slowly with increasing temperature, and continues to decrease well above T_C [Fig. 4(f)]. This suggests that the probability of dd hopping processes scales with the spin-spin correlation length, which will be gradually suppressed with increasing temperature above T_C where short-range spin fluctuations are known to persist [40–42].

Furthermore, we find that the Cr-derived states measured in ARPES exhibit a particularly large increase in lifetime upon cooling through T_C. While this is already evident from a pronounced reduction in linewidth of both the Cr t_{2g} and hybridized $5p$-e_g states at the Γ point (Fig. 4), it is particularly apparent for a somewhat more dispersive state 0.8 eV below the valence band maximum at the T point, shown in Fig. 5. The relatively steep in-plane dispersion of this state likely reflects finite hybridization with Te $5p$ orbitals, where they become nearly degenerate with the Cr t_{2g} states. While the Te $5p_{x,y}$ states at the valence band top exhibit only weak linewidth changes with increasing temperature, the linewidth of this hybridized Cr-Te state increases by more than a factor of two at the ferromagnetic transition [Figs. 5(d) and 5(e)]. Although it is normal for ARPES spectra to display temperature-dependent linewidths due to electron-phonon
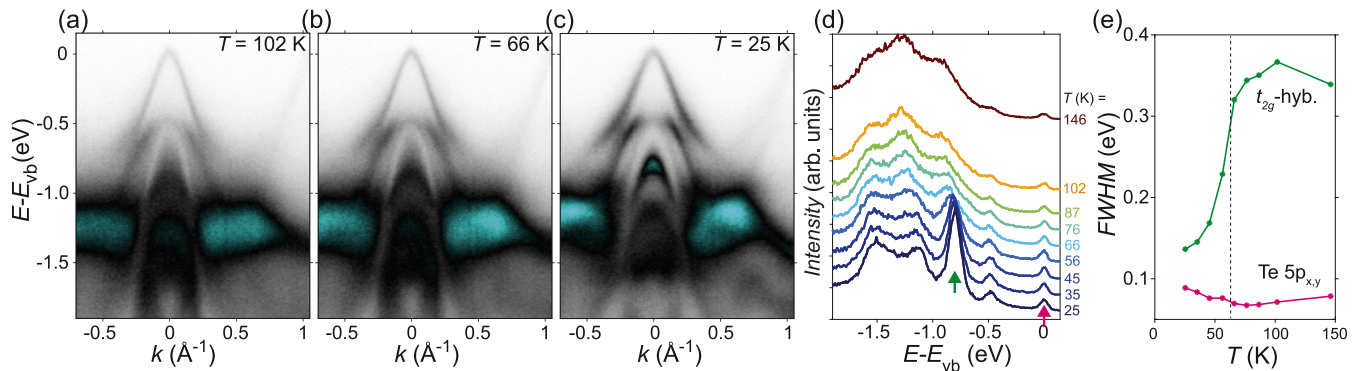
FIG. 5. Lifetime enhancements below T_C. (a)–(c) Temperature-dependent ARPES measurements at the T point ($h\nu = 61$ eV) at temperatures of (a) 102 K, (b) 66 K, and (c) 25 K. (d) Corresponding EDCs at the T point. (e) The extracted full width at half maximum of the uppermost t_{2g} state, determined from fits to these EDCs, shows a remarkable sharpening upon cooling thought the ferromagnetic ordering transition. This indicates a pronounced increase in lifetime of this state, in contrast to the almost temperature-independent lifetime of the uppermost valence band states. For fit details, see Fig. SM3 in SM [14].

coupling and other scattering mechanisms, the magnitude of the change here is remarkable. We attribute this to a much reduced probability of spin-flip scattering in the ferromagnetic state, where the spins are aligned, pointing to a significant influence of magnetic fluctuations on shaping the underlying electronic structure of the paramagnetic state. The particular sensitivity of the state identified here likely reflects its more substantial degree of itinerancy, and thus a more extensive wave function, which will exhibit greater sensitivity to longer-range spin alignment. Furthermore, our observations show an interesting correspondence with the substantial increase in phonon lifetimes below T_C as reported by Raman scattering measurements [43], suggesting that electron-phonon as well as spin-phonon scattering could contribute to that effect.

IV. CONCLUSIONS

Overall, our ARPES measurements reveal distinct temperature-dependent energy shifts and linewidth changes that are linked, in different ways, to the onset of ferromagnetic ordering. On the scale of the whole bandwidth, however, it is worth observing that the spectral functions of the ferromagnetic and paramagnetic states show a similar global structure. This implies that the Cr sites retain a local and instantaneous spin polarization even in the paramagnetic phase. Thus, as a starting point, the local moment perspective can be used as for $CrGeTe_3$ and related materials. However, the Cr 3d states also have significant dispersions, hybridize strongly with the Te 5p orbitals where allowed by symmetry, and display rich and complex temperature-dependent signatures in our experimental electronic structure measurements, exposing the limitations of the local moment picture. Nevertheless, by combining the analysis of the orbital character of states and energy shifts through T_C, one can obtain unique insights into the superexchange mechanism.

Due to the structural similarity between $CrGeTe_3$ and the CrX_3 family, we expect the ideas developed here to be applicable also in the trihalides. Indeed, it is notable that the magnetic ordering temperature in that family increases with increasing covalency: from 16 K in $CrCl_3$ to 61 K in CrI_3 [4,44], while a

substantial occupation of Cr e_g orbitals has also been detected in CrI_3 [34]. Excitingly, high-quality ARPES measurements can now be performed on exfoliated flakes of 2D materials [45,46]. Thus the spectroscopic approach outlined here opens powerful new routes to study how the magnetic ordering tendencies evolve when the material is thinned to the few-layer limit, where T_C is known to be strongly suppressed [2]. We have shown how ARPES measurements provide direct access to the energy scales ultimately underpinning the formation of ferromagnetism; the observation of temperature-dependent band shifts such as those observed here will thus allow determining whether the driving force for ferromagnetism is weakened when interlayer coupling is removed or whether the suppression of T_C can instead be attributed to the growth of fluctuations in the 2D limit. More generally, the results shown here indicate how an experimental band-structure perspective can give important insight even in a "local moment" magnetic system.

[1] B. Huang, G. Clark, E. Navarro-Moratalla, D. R. Klein, R. Cheng, K. L. Seyler, D. Zhong, E. Schmidgall, M. A. McGuire, D. H. Cobden, W. Yao, D. Xiao, P. Jarillo-Herrero, and X. Xu, Nature (London) **546**, 270 (2017).

[2] C. Gong, L. Li, Z. Li, H. Ji, A. Stern, Y. Xia, T. Cao, W. Bao, C. Wang, Y. Wang, Z. Q. Qiu, R. J. Cava, S. G. Louie, J. Xia, and X. Zhang, Nature (London) **546**, 265 (2017).

[3] K. S. Burch, D. Mandrus, and J.-G. Park, Nature (London) **563**, 47 (2018).

[4] H. Li, S. Ruan, and Y.-J. Zeng, Adv. Mater. **31**, 1900065 (2019).

[5] X. Wang, J. Tang, X. Xia, C. He, J. Zhang, Y. Liu, C. Wan, C. Fang, C. Guo, W. Yang, Y. Guang, X. Zhang, H. Xu, J. Wei, M. Liao, X. Lu, J. Feng, X. Li, Y. Peng, H. Wei, R. Yang, D. Shi, X. Zhang, Z. Han, Z. Zhang, G. Zhang, G. Yu, and X. Han, Sci. Adv. **5**, eaaw8904 (2019).

[6] M. Gibertini, M. Koperski, A. F. Morpurgo, and K. S. Novoselov, Nat. Nanotechnol. **14**, 408 (2019).

[7] C. Gong and X. Zhang, Science **363**, eaav4450 (2019).

[8] V. Carteaux, D. Brunet, G. Ouvrard, and G. Andre, J. Phys.: Condens. Matter **7**, 69 (1995).

[9] H. Ji, R. A. Stokes, L. D. Alegria, E. C. Blomberg, M. A. Tanatar, A. Reijnders, L. M. Schoop, T. Liang, R. Prozorov, K. S. Burch, N. P. Ong, J. R. Petta, and R. J. Cava, J. Appl. Phys. **114**, 114907 (2013).

[10] Y. Liu and C. Petrovic, Phys. Rev. B **96**, 054406 (2017).

[11] B. Siberchicot, S. Jobic, V. Carteaux, P. Gressier, and G. Ouvrard, J. Phys. Chem. **100**, 5863 (1996).

[12] D. C. Freitas, R. Weht, A. Sulpice, G. Remenyi, P. Strobel, F. Gay, J. Marcus, and M. Núñez-Regueiro, J. Phys.: Condens. Matter **27**, 176002 (2015).

[13] M. A. McGuire, Crystals **7**, 121 (2017).

[14] See Supplemental Material at http://link.aps.org/supplemental/10.1103/PhysRevB.101.205125 for sample characterization, details of the fit procedure, and comparison of the XMCD data to a Cr_2O_3 reference sample.

[15] G. van der Laan and A. I. Figueroa, Coord. Chem. Rev. **277-278**, 95 (2014).

[16] B. T. Thole, G. van der Laan, J. C. Fuggle, G. A. Sawatzky, R. C. Karnatak, and J.-M. Esteva, Phys. Rev. B **32**, 5107 (1985).

[17] G. van der Laan, Hitchhiker's guide to multiplet calculations, in *Magnetism: A Synchrotron Radiation Approach* (Springer, Berlin, Heidelberg, 2006), pp. 143–199.

[18] G. van der Laan and B. T. Thole, Phys. Rev. B **43**, 13401 (1991).

[19] R. D. Cowan, *The Theory of Atomic Structure and Spectra* (University of California Press, Berkeley, 1981).

[20] K. Yaji, A. Kimura, C. Hirai, M. Taniguchi, M. Koyama, H. Sato, K. Shimada, A. Tanaka, T. Muro, S. Imada, and S. Suga, Phys. Rev. B **70**, 064402 (2004).

[21] J. Zhang, X. Cai, W. Xia, A. Liang, J. Huang, C. Wang, L. Yang, H. Yuan, Y. Chen, S. Zhang, Y. Guo, Z. Liu, and G. Li, Phys. Rev. Lett. **123**, 047203 (2019).

[22] M. Suzuki, B. Gao, K. Koshiishi, S. Nakata, K. Hagiwara, C. Lin, Y. X. Wan, H. Kumigashira, K. Ono, S. Kang, S. Kang, J. Yu, M. Kobayashi, S.-W. Cheong, and A. Fujimori, Phys. Rev. B **99**, 161401(R) (2019).

[23] Y. F. Li, W. Wang, W. Guo, C. Y. Gu, H. Y. Sun, L. He, J. Zhou, Z. B. Gu, Y. F. Nie, and X. Q. Pan, Phys. Rev. B **98**, 125127 (2018).

[24] W. Jiang, Z. Yang, Y. Li, G. Wang, Q. Jing, D. Guan, J. Ma, W. Zhang, and D. Qian, J. Appl. Phys. **127**, 023901 (2020).

[25] M. D. Watson, O. J. Clark, F. Mazzola, I. Marković, V. Sunko, T. K. Kim, K. Rossnagel, and P. D. C. King, Phys. Rev. Lett. **122**, 076404 (2019).

[26] K. Shimada, T. Saitoh, H. Namatame, A. Fujimori, S. Ishida, S. Asano, M. Matoba, and S. Anzai, Phys. Rev. B **53**, 7673 (1996).

[27] Multiple bands are expected here as the t_{2g} manifold is split by trigonal distortions, and because there are two inequivalent Cr sites in the unit cell.

[28] V. Sunko, F. Mazzola, S. Kitamura, S. Khim, P. Kushwaha, O. J. Clark, M. D. Watson, I. Marković, D. Biswas, L. Pourovskii, T. K. Kim, T.-L. Lee, P. K. Thakur, H. Rosner, A. Georges, R. Moessner, T. Oka, A. P. Mackenzie, and P. D. C. King, Sci. Adv. **6**, eaaz0611 (2019).

[29] V. Korenman and R. E. Prange, Phys. Rev. Lett. **53**, 186 (1984).

[30] J. B. Staunton, A. Marmodoro, and A. Ernst, J. Phys.: Condens. Matter **26**, 274210 (2014).

[31] S. Kang, S. Kang, and J. Yu, J. Electron. Mater. **48**, 1441 (2019).

[32] G. Menichetti, M. Calandra, and M. Polini, 2D Mater. **6**, 045042 (2019).

[33] L. B. Duffy, A. I. Figueroa, L. Gładczuk, N.-J. Steinke, K. Kummer, G. van der Laan, and T. Hesjedal, Phys. Rev. B **95**, 224422 (2017).

[34] A. Frisk, L. B. Duffy, S. Zhang, G. van der Laan, and T. Hesjedal, Mater. Lett. **232**, 5 (2018).

[35] D.-H. Kim, K. Kim, K.-T. Ko, J.-H. Seo, J. S. Kim, T.-H. Jang, Y. Kim, J.-Y. Kim, S.-W. Cheong, and J.-H. Park, Phys. Rev. Lett. **122**, 207201 (2019).

[36] For the idealized case, with perfect octahedra and $90°$ bond angles, the formation of such σ bonds is strictly forbidden by symmetry.

[37] J. Kanamori, J. Phys. Chem. Solids **10**, 87 (1959).

[38] K. Wang, S. Nikolaev, W. Ren, and I. Solovyev, Phys. Chem. Chem. Phys. **21**, 9597 (2019).

[39] A. Ron, S. Chaudhary, G. Zhang, H. Ning, E. Zoghlin, S. D. Wilson, R. D. Averitt, G. Refael, and D. Hsieh, arXiv:1910.06376.

[40] T. J. Williams, A. A. Aczel, M. D. Lumsden, S. E. Nagler, M. B. Stone, J.-Q. Yan, and D. Mandrus, Phys. Rev. B **92**, 144404 (2015).

[41] J. Zeisner, A. Alfonsov, S. Selter, S. Aswartham, M. P. Ghimire, M. Richter, J. van den Brink, B. Büchner, and V. Kataev, Phys. Rev. B **99**, 165109 (2019).

[42] A. Ron, E. Zoghlin, L. Balents, S. D. Wilson, and D. Hsieh, Nat. Commun. **10**, 1654 (2019).

[43] Y. Tian, M. J. Gray, H. Ji, R. J. Cava, and K. S. Burch, 2D Mater. **3**, 025035 (2016).

[44] M. Abramchuk, S. Jaszewski, K. R. Metz, G. B. Osterhoudt, Y. Wang, K. S. Burch, and F. Tafti, Adv. Mater. **30**, 1801325 (2018).

[45] I. Cucchi, I. Gutiérrez-Lezama, E. Cappelli, S. McKeown Walker, F. Y. Bruno, G. Tenasini, L. Wang, N. Ubrig, C. Barreteau, E. Giannini, M. Gibertini, A. Tamai, A. F. Morpurgo, and F. Baumberger, Nano Lett. **19**, 554 (2019).

[46] P. V. Nguyen, N. C. Teutsch, N. P. Wilson, J. Kahn, X. Xia, A. J. Graham, V. Kandyba, A. Giampietri, A. Barinov, G. C. Constantinescu, N. Yeung, N. D. M. Hine, X. Xu, D. H. Cobden, and N. R. Wilson, Nature (London) **572**, 220 (2019).

[47] University of St Andrews Research Portal. https://doi.org/10.17630/8eb18480-6d2c-48f4-9e5e-49357a9d26c2.